Journal of Solid State Electrochemistry (2022) 26:2479–2489
https://doi.org/10.1007/s10008-022-05257-0

ORIGINAL PAPER

Reclaimed δ-MnO_2 from exhausted Zn/C primary cells as active cathode in secondary Zn^{2+} ion batteries

M. A. García-López[1] · M. T. Oropeza-Guzmán[2] · J. C. Calva-Yáñez[3]

Received: 6 July 2022 / Revised: 19 July 2022 / Accepted: 22 July 2022 / Published online: 12 August 2022

Abstract

This work presents the construction of a reversible zinc ion battery using components recovered from exhausted Zn/C primary cells. The reduced cathode material from the primary battery served as raw material to synthesize birnessite-type manganese oxide, which, when working as a cathode in conjunction with an aqueous electrolyte and a recovered zinc anode, exhibits a reversible capacity of 289 mAh g^{-1} at 20 mA g^{-1}. This performance is similar to that observed for manganese oxide synthesized from potassium permanganate reagent (270 mAh g^{-1} at 20 mA g^{-1}). The structural characterization shows that the material obtained from recycling activities changes its morphology and surface area due to the presence of sodium ions during the synthesis process, and these remain in their structure. These changes promote a 60% capacity lost after being cycled at different charges, compared to 26% of δ-MnO_2 synthesized from permanganate reagent. The long-term stability test shows that both batteries can retain their capacity after 1000 discharge/charge cycles at a load of 1000 mA g^{-1}. The results support the sustainability of using a primary cell residue to get an electric energy storage device again.

Keywords Recycling of exhausted Zn/C batteries · Electrochemical energy storage · Zinc ion batteries · Manganese oxide

Introduction

Energy storage is essential for developing and growing sustainable generation technologies, which point to alleviating climate change. Solar radiation and wind force have the potential to meet the growing electricity demand. However, due to the intermittent nature of the energy sources, it is necessary to have storage devices that can save the surplus of energy produced and deliver it to the grid when needed or provide power for stationary and mobile applications. Electrochemical energy storage devices such as secondary ion batteries [1–3], capacitors/supercapacitors [1, 4, 5], flow batteries [6, 7], and liquid metal batteries [8] can satisfy all these needs. Secondary batteries are devices based on reversible electrochemical reactions. Pb-acid accumulators, Ni–Cd, Ni–Fe, Ni-Zn, nickel metal hydride (NMH), and alkali ion (Li-ion) batteries are standard configurations. Li-ion batteries are electrical energy storage devices that use lithium salt as an electrolyte that provides the ions necessary for the reversible electrochemical reaction between the cathode and the anode. They are lightweight devices with high energy capacity that can operate for a high number of regeneration cycles [1]. Based on the principles of energy storage and conversion of Li-ion batteries and existing technology, earth-abundant ions such as Na^+ [9, 10], K^+ [11, 12], and Mg^{2+} [13, 14] are used for energy storage. However, these systems suffer from the same problems as the Li^+ ion regarding safety, processing costs, and environmental compatibility [1, 2]. At a practical level, the main drawback when assembling these devices is the reactivity of these alkaline and alkaline earth metal ions in the presence of humidity. Therefore, assembling the batteries under controlled environmental conditions is necessary to guarantee their maximum effectiveness. Similarly alkaline ions, the Zn^{2+} ion is used for energy storage using the intercalation/de-intercalation principle [15].

✉ J. C. Calva-Yáñez
jccalva@conacyt.mx

1 Universidad Politécnica del Estado de Guerrero, Ingeniería en Tecnología Ambiental, Carr. Fed. Iguala-Taxco Km 105 Puente Campuzano, 40321 Taxco de Alarcón, Gro., Mexico

2 Instituto Tecnologico de Tijuana, Blvd Alberto Limón Padilla s/n Col. Otay-Tecnologico, 22510 Tijuana, B.C, Mexico

3 CONACyT-Tecnológico Nacional de México/I.T. Tijuana, Centro de graduados e Investigación en Química, Blvd. Alberto Limón Padilla s/n Col. Otay-Tecnológico, B.C. 22510 Tijuana, Mexico

Material science researchers have recently increased their efforts in developing secondary zinc-ion batteries (ZIB) using aqueous electrolytes [15–21]. This fact opens the possibility of manufacturing safe and environmentally friendly devices and reducing processing costs. The system of a ZIB consists of a metallic Zn anode, an aqueous electrolyte containing Zn ions, and a cathode based on a host material capable of storing zinc ions. The battery operation consists of two reversible electrochemical processes: (i) during discharge, the zinc from the anode is oxidized to Zn^{2+} ions, diffuses into the electrolyte, and intercalates in the tunnels of the host material in the cathode, interacting with the flow of electrons from the external circuit; (ii) in the charging process, the electron excess in the cathode and generated Zn^{2+} ions diffuse into the electrolyte and are deposited in the metallic Zn anode when interacting with electrons from the external circuit [8, 17, 22]. These two processes involve the participation of Zn^{2+} ions in the electrolyte, connecting the host material with the metallic Zn to produce the rechargeable battery. Although metallic Zn can provide a capacity of 820 mAh g^{-1} [15], the determining factor in the energy storage capacity of a secondary battery is the amount of insertion and disinsertion of the host ion occurring on the cathode. In the last years, intense research has been carried out to obtain active materials for ZIB cathodes with high storage capacity, highlighting MnO_2 (285 mAh g^{-1}) [15, 17, 22], Co_3O_4 (162 mAh g^{-1}) [23], $ZnMnO_4$ (150 mAh g^{-1}) [24], $Na_3V_2(PO_4)_3$ (97 mAh g^{-1}) [25], and some Prussian blue analogs ($\ll$ 60 mAh g^{-1}) [26]. However, manganese dioxide is still the focus of research due to its abundance, low cost, and minimum toxicity. MnO_2 polymorphism makes it an interesting candidate for ion storage due to its octahedral structure with 1×1, 2×2, and 1×2 one-dimensional channels or tunnels of the α, β, and γ phases, and the lamellar structure of the δ phase [15, 17, 22, 27–29]; all of them are ideal structures for zinc ion storage.

Electrochemical devices have developed into a dependable source of electrical energy since the end of the eighteenth century. From the galvanic cells, it was possible to generate the electrical charges necessary to carry out the oxidation–reduction process that led to significant scientific advances. The use of Zn and MnO_2 for power supply applications dates back to 1865 when the Leclanché Zn-MnO_2 wet cell was introduced. The Zn-MnO_2 cells obtain their energy from the irreversible chemical oxidation reaction of the Zn anode and the irreversible reduction of the MnO_2 cathode. In the modern Zn-MnO_2 primary cells, an acidic aqueous paste of $ZnCl_2$ or alkaline KOH is used as an electrolyte. In the first case, the electrolyte is mixed with the MnO_2 powder in the cathode, while in alkaline batteries, the anode is composed of a dispersion of zinc powder in a gel containing potassium hydroxide. Both devices have a voltage of 1.5 V per cell, although alkaline batteries have a higher energy density and a longer life; the two types of batteries are widely used in portable electronic devices [30]. Primary Zn/MnO_2 batteries are the world's most widely used disposable energy storage devices. The global alkaline battery market was worth 17.3 billion in 2019 and is expected to grow at a compound annual growth rate of 9.22% by 2023 [31]. Once these devices have exhausted their useful life, they must be disposed of and treated as hazardous solid waste. The treatment of this waste is usually grinding and leaching to recover the elements of commercial value for possible applications in the iron and steel, metal, or ceramic industries or to make new primary cells. A little-explored proposal is the recovery of the components of the primary Zn/C batteries to obtain the raw materials for manufacturing secondary batteries of the ZIB type. This work proposes to reuse the exhausted cathode paste of primary Zn/MnO_2 cells and, following a simple route, obtain the active cathode material for secondary ZIB and compare it with material prepared from chemical reagents. All this is to compare the efficiency in the storage of renewable energy with the view to sustainability.

Experimental

Reagents

Oxalic acid di-hydrated ($H_2C_2O_4$ $2H_2O$ Sigma-Aldrich 98%), sodium carbonate (Na_2CO_3 Sigma-Aldrich 99.5%), methyl acetate (CH_3COOCH_3 Sigma-Aldrich 98%), poly(vinylidene fluoride) (Sigma-Aldrich $M_W \sim 534{,}000$), and N-methyl-2-pyrrolidone (C_5H_9NO Sigma-Aldrich 99%), sulfuric acid (H_2SO_4 FAGA lab 98%), potassium permanganate ($KMnO_4$ FAGA lab 99%), and isopropanol ($(CH_3)_2CHOH$ FAGA lab 99%). Potassium carbonate (K_2CO_3 Jalmek 98%) and zinc sulfate heptahydrate ($ZnSO_4$ $7H_2O$ Jalmek 99%), hydrochloric acid (HCl Fermont 36%), manganese (II) sulfate monohydrate ($MnSO_4$ xH_2O Fermont 98%), bleaching solution (NaClO Blancatel 45 g L^{-1}). All aqueous solutions were prepared with Milli-Q® water (18 MΩ, Thermo Scientific®).

Recycling exhausted Zn/C cells

The synthesis of $KMnO_4$ produced by reusing the cathode paste of depleted primary Zn/C cells is briefly addressed. First, the exhausted Zn/C cells are disassembled, and the

Zn foil, graphite bar, and spend cathode paste (mainly composed of MnO(OH), carbon powder, and electrolyte salts) are recovered. The paste is washed with distilled water, filtered, rinsed with deionized water, and dried at 100 °C overnight. The carbon content in the dry paste was determined by weighting the residue of different batches after thermal annealing at 600 °C for 3 h.

The recovery of manganese as a soluble salt was accomplished by reacting the dry paste with sufficient amounts of concentrated sulfuric acid and di-hydrated oxalic acid following reaction (1) and filtering the solution to remove the insoluble carbon particles. The manganese (II) precipitation is carried out with sodium carbonate according to reaction (2).

$$2MnOOH + HO_2CCO_2H + 2H_2SO_4 \rightarrow 2MnSO_4 + 2CO_2 + 4H_2O \quad (1)$$

$$MnSO_4 + Na_2CO_3 \rightarrow MnCO_3 \downarrow + Na_2SO_4 \quad (2)$$

The precipitated manganese carbonate is then filtered and washed with deionized water and dried at 80 °C overnight. To synthesize potassium permanganate, the dried $MnCO_3$ was reacted with the necessary amounts of potassium carbonate and commercial sodium hypochlorite solution (45 g L^{-1}) under vigorous stirring and heated until the color changed to intense violet, following reaction (3).

$$2MnCO_3 + 5NaClO + K_2CO_3 \rightarrow 2KMnO_4 + 5Nacl + 3CO_2 \quad (3)$$

The heating was maintained until the solution volume was reduced to one fourth of the original, then hot filtered through a glass filter, cooled down, and kept at 5 °C for 48 h. The precipitated crystals of the mixture $KMnO_4$/NaCl are separated from the mother liquors, dried, and recrystallized, redissolving them in deionized water and cooling down the solution to −3 °C. Finally, the crystals are dried and preserved for later use. Mn, K, and Na content in the obtained material was later determined.

Synthesis of δ-MnO_2 nanostructures

For the synthesis of δ-MnO_2 nanostructures [32], $KMnO_4$ (crystallized and reagent) and methyl acetate were employed. Eighty-five milliliters of 20 mM aqueous solution of $KMnO_4$ and 41 mL of methyl acetate were added into a 250 mL flat bottom round flask. The mixture is heated at 60 °C and kept at reflux conditions for 2 h under continuous stirring. After the reaction time has elapsed, the MnO_2 dispersion is transferred to a separatory funnel, precipitated, and separated from the organic/aqueous biphasic part; washed with D.I. water, 0.1 M of HCl, and isopropanol; and dried at 50 °C for 48 h in air.

Material characterization

Mn, K, and Na content in the crystallized $KMnO_4$ was determined by Inductively Coupled Plasma Optic Emission Spectroscopy (ICP-OES; Perkin-Elmer Optima 8300). The morphology of MnO_2 was analyzed by field emission scanning electron microscopy (JEOL, JSM-7800F Prime). Semi-quantitative chemical analysis was carried out by Energy-dispersive X-ray spectroscopy (Bruker, Quantax EDS). Phase and structure were identified by powder X-ray diffraction (Philips, X'Pert MPD) employing Cu Kα ($\lambda = 0.1506$ nm) rotation from 5 to 70°. The surface area and textural properties were determined by N_2 adsorption–desorption isotherms using the Non-Linear Density Functional Theory GCMC: Grand Canonical Monte Carlo method (Quantachrome Instruments Autosorb-iQ).

Electrochemical measurements

The electrochemical performance was tested in 5.067-cm^2 Swagelok-type cells using a potentiostat/galvanostat (Biologic, VMP-300). The working electrodes were fabricated by blending δ-MnO_2 powder, conductive carbon, and poly(vinylidene fluoride) (PVDF) in a weight ratio of 8:1:1 using N-methyl-2-pyrrolidone as a solvent. The obtained slurry was brush coated onto a carbon foil and placed on a heating grid for 60 min at 250 °C with a heating ramp of 10 °C min^{-1}. The loading mass of active material was ~ 1.8 mg cm^{-2}. Fiberglass paper and recycled zinc foil were employed as the separator and anode, respectively. As an electrolyte, a 1 M $ZnSO_4$/0.05 M $MnSO_4$ aqueous solution was used. Cyclic voltammetry (CV) was performed at a scan rate of 0.5 mV s^{-1} from 0.8 to 2.0 V. Electrochemical impedance spectroscopy (EIS) was performed with an AC perturbation signal of 10 mV, and the frequency ranged from 100 kHz to 100 mHz. Galvanostatic charge–discharge curves were studied through battery capacity determination (BCD) analysis in the same potential as CV.

Results and discussion

Analysis of Mn, K, and Na on exhausted paste and crystalized $KMnO_4$

The thermal treatment of the cathodic pastes from exhausted primary acid Zn/MnO_2 cells was carried out under an air atmosphere at 600 °C for 3 h, weighing the final residue. The analyses were performed by battery

Table 1 Results of elemental ICP-EOS analysis for $KMnO_4$ crystallized (_c) and reagent (_r)

Sample	Mn/K mass ratio	Mn:K mol ratio	Mn/Na mass ratio	Mn:Na mol ratio
$KMnO_4$_c	1.35/1	1:0.961	1.06/1	1:2.05
$KMnO_4$_r	1.398/1	1:0.995	0	0

brands (i.e., Panasonic©, Eveready©, Rocket©). The obtained results show a final average percentage of 70% of the original mass consisting of MnO_2. After following the experimental procedure detailed in the previous section, crystallized $KMnO_4$ was obtained. Mn/Na and Mn/K mass and molar ratios of crystallized $KMnO_4$ were determined from the ICP analysis and compared with the $KMnO_4$ reagent (Table 1).

The molar ratios of the material obtained through the crystallization process are slightly lower than the reaction (3) stoichiometry due to the higher solubility of sodium chloride in aqueous media compared with potassium permanganate under the crystallization conditions, which causes it remains in the mother liquor.

Morphology and semi-quantitative chemical composition analysis

Crystallized and reagent $KMnO_4$ were used as raw materials for the interfacial synthesis of MnO_2. The morphologies of the synthesized materials are shown in Fig. 1. The MnO_2 produced from crystallized $KMnO_4$ shows a quasi-spherical morphology with some projections like nanowires surrounding the particle (Fig. 1a). A closer view allows us to observe the shape of the hemispherical particles with diameters between 60 and 150 nm (Fig. 1b). In comparison, the MnO_2 synthesized from $KMnO_4$ reagent presents morphology-like sheets with projections similar to those observed in the previously described material (Fig. 1c); a magnification allows us to observe sheets that can be found with lengths from 150 to more than 700 nm (Fig. 1d).

EDS analyses are summarized in Table 2. The atomic percent for Mn, O, K, and Na were measured in different zones to get an average value. The percentages obtained for the samples are presented before and after washing them with 0.1 M HCl solution (δ-MnO_2_c, δ-MnO_2_r, and δ-MnO_2_C, δ-MnO_2_R, respectively). High percentages of K and Na are observed in the sample synthesized from crystallized

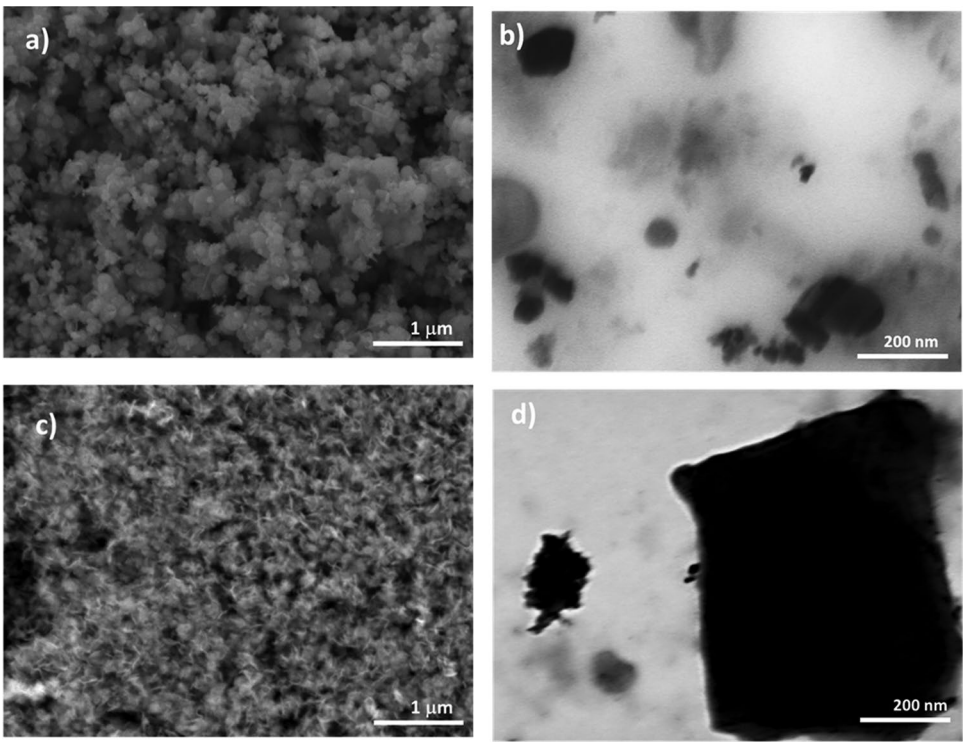

Fig. 1 FE-SEM images of synthesized δ-MnO_2: **a** and **b** crystallized $KMnO_4$ (δ-MnO_2_C) and **c** and **d** reagent $KMnO_4$ (δ-MnO_2_R)

Table 2 Semi-quantitative chemical data from EDS analysis of synthesized materials before and after treatment with 0.1 M HCl

Sample	% Mn	% O	% K	% Na	Mn/K ratio	Mn/Na ratio
δ-MnO_2_c	18.71	73.23	2.58	5.48	7.25/1	3.41/1
δ-MnO_2_C	23.51	74.69	0.56	1.24	42/1	19/1
δ-MnO_2_r	19.83	77.39	2.78	0	7.1/1	0
δ-MnO_2_R	33.24	62.48	4.38	0	7.6/1	0

$KMnO_4$. The presence of sodium in the precursor $KMnO_4$ solution promotes the formation of δ-MnO_2 with spherical morphology (accumulation of small sheets of δ-MnO_2), while when $KMnO_4$ reagent is used, the characteristic laminar structure from interfacial synthesis is obtained. The washing of both materials with 0.1 M of HCl solution has different effects. While in the material synthesized from the crystallized $KMnO_4$, a critical reduction in the content of K and Na is observed, in the material synthesized from the $KMnO_4$ reagent, the change in the Mn/K ratio is minimal, indicating that the potassium ion present in this material was not accessible for removal as KCl.

Phase and structure

The surface area, pore size, and volume of pores of synthesized materials that were measured by the physisorption of nitrogen at 77 K are presented in Fig. 2. The obtained isotherms for both δ-MnO_2 nanostructures have the characteristic IV type shape with H_3 hysteric loops in the range of 0.2–0.95 P/P_0, indicating the existence of complex pore structures with networking significant effects, where adsorption metastability and desorption branch are delayed as pore blocking and cavitation associated with pore evaporation in networked structures take place (ink-bottle-pores) [33]. DFT method was used to determine the pore size distribution and surface area. It is observed that the average pore size distribution varies in both samples. The MnO_2 synthesized from crystallized permanganate solution shows a uniform pore size distribution with diameters in the range of 2–5 nm, while in the MnO_2 produced from permanganate reagent solution, the presence of a mixture of micropores and mesopores whose diameters range from 2 to more than 18 nm is observed. Surface area, pore volume, and half pore width (HPW) for both materials are summarized in Table 3. The surface area for the material with sheet-like morphology is close to 220 $m^2\ g^{-1}$, while the spherical shape is only 82.3 $m^2\ g^{-1}$. The pore volume and half pore width are more significant than those measured for hemispherical morphology material.

The X-ray diffraction patterns (Fig. 3) of synthesized materials show the reflection characteristics for monoclinic δ-MnO_2 made up of loosely bound layers of edge-shared MnO_6 located at (001) planes (JCPDS 80–1098). The diffraction peaks at 12.2°, 24.8°, 37°, and 66° of 2θ indicate the (001), (002), (110), and (310) crystal planes of δ-MnO_2, corresponding to a basal spacing of 0.73 nm. The broadening and intensity of the diffraction peaks indicate that the δ-MnO_2 prepared from permanganate reagent solution is more crystalline than that synthesized from crystallized $KMnO_4$. The lattice constants for δ-MnO_2_C are $a = 0.5147$ nm, $b = 0.2832$ nm, $c = 0.7171$ nm, and $\beta = 103.7°$, while $a = 0.5136$ nm, $b = 0.2827$ nm, $c = 0.7248$ nm, and $\beta = 102.8°$ for δ-MnO_2_R. Parameter c corresponds to the spacing between MnO_6 monolayers. The anisotropic growth in the axial direction b/c is 2.533 and 2.564 for δ-MnO2_C and δ-MnO2_R, respectively. The slight elongation of the crystals in the c axis for δ-MnO2_R may be due to the sheet-like morphology. The apparent density of the synthesized materials was determined from the bulk density, calculated from lattice constants, and the pore volume obtained from physisorption characterization. Table 4 summarizes the anisotropic growth, crystal size, calculated bulk, and apparent densities.

Electrochemical characterization

The electrochemical performance of prepared cathodes was evaluated in a 0.5-inch Swagelok-type cell (electrode area 1.2968 cm^2) with a recovered Zn sheet acting as counter and reference electrode, fiberglass paper as the separator, and a 1 M $ZnSO_4$/0.05 M $MnSO_4$ aqueous solution as electrolyte. Cyclic voltammograms were performed in a potential range from 0.8 to 2 V vs Zn^{2+}/Zn at a scan rate of 0.5 mV s^{-1} (Fig. 4a, b). The open circuit voltage for as-assembled cells was 1.36 V and

Table 3 Specific surface area, pore volume, and pore size of synthesized δ-MnO_2

Sample	S.A. ($m^2\ g^{-1}$)	P.V. ($cm^3\ g^{-1}$)	H.P.W. (nm)
δ-MnO_2_C	82.313	0.27	3.72
δ-MnO_2_R	222.59	1.63	18

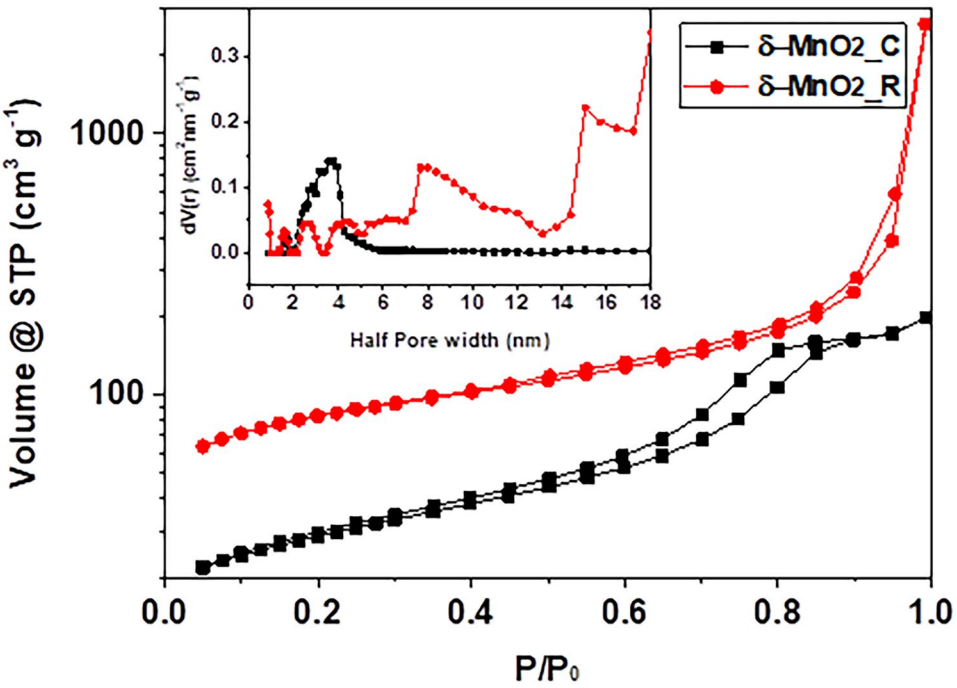

Fig. 2 Isotherms of nitrogen adsorption–desorption and pore size distribution plot (inset) of synthesized δ-MnO_2

1.39 V for cathodes with δ-MnO_2_C and δ-MnO_2_R as active materials, respectively. The initial sweep shows, in both cases, the formation of an oxidation peak at 1.6 V, consistent with the potential for extracting Zn^{2+} ions from the lamellar structure of δ-MnO_2 and two reduction peaks. The first one is related to the potential for insertion of Zn^{2+} ions into the host structure (1.28 and 1.31 V for δ-MnO_2_C and δ-MnO_2_R, respectively),

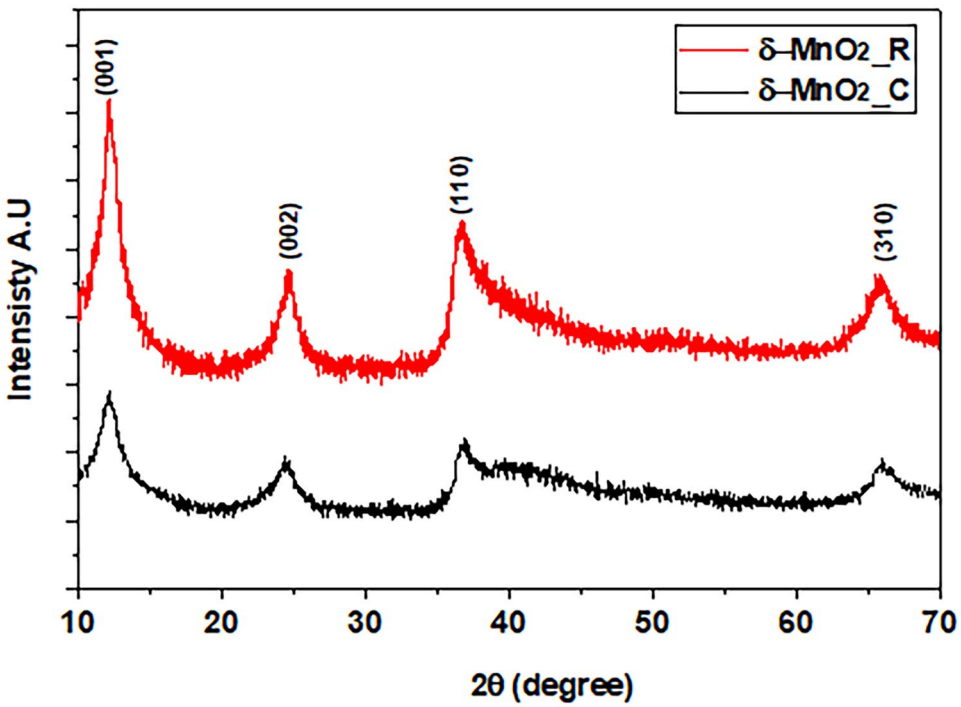

Fig. 3 X-ray diffraction patterns of synthesized δ-MnO_2 synthesized from crystallized and reagent $KMnO_4$ solutions

Table 4 Anisotropic growth *b*/*c* ratio, calculated density from XRD data, and the apparent density (ρ^*)

Sample	*b*/*c* ratio	Crystal size (nm)	ρ (g cm^{-3})	ρ^* (g cm^{-3})
δ-MnO_2_C	2.533	5.18	3.365	1.76
δ-MnO_2_R	2.564	4.92	3.353	0.518

and the second one is related to the reduction potential for Mn^{4+} to the Mn^{3+}/Mn^{2+} states (1.1 and 1.15 V for δ-MnO_2_C and δ-MnO_2_R, respectively). The displacement of the signal for Mn^{4+} reduction is consistent with the difference in potential for inserting Zn^{2+} ions into the host material. The large capacitive current present in the δ-MnO_2_C electrode at the end of the first electrochemical sweep cycle can be associated with the morphology and surface area of active material available for ion adsorption (Fig. 4a). After ten cycles of electrochemical scanning, the increase in oxidation and reduction peak currents for the δ-MnO_2_C cathode is probably due to gradual electrode activation, shifting the maximum of the oxidation and reduction peaks to 1.64 and 1.3 V, respectively. The peak associated with the transition of Mn^{4+} to a less oxidized state is significantly reduced by 50 mV. This fact lets us assume that a stable state on insertion/de-insertion of Zn^{2+} into the host material has been reached. In the case of δ-MnO_2_R, there is no significant increase in the capacitive current of the electrode, although textural analyses show that the δ-MnO_2_R material has a larger surface area. The arrangement of δ-MnO_2_R sheets onto the current collector is assumed to be stacked perpendicularly to the surface. If so, this geometric arrangement restricts the surface area available for the adsorption of Zn^{2+} ions, limiting the discharge process to the diffusion within the δ-MnO_2 tunnels. After tenth sweeping cycles, the oxidation peak becomes broader due to the presence of a shoulder at 1.54 V with the maximum at 1.61 V and may correspond to the reinstatement of the Mn^{4+} state accompanied by the Zn^{2+} extraction [34]. The reduction peak is shifted to 1.33 V while the peak associated with the reduction of Mn^{4+} almost disappears, reaching the stable state for insertion/de-insertion of Zn^{2+} (Fig. 4b).

The galvanostatic discharge/charge curves were performed by the BCD technique. Figure 5a shows the profiles of the δ-MnO_2_C cathode in the potential range of 0.9–1.9 V vs Zn^{2+}/Zn at different loads and demands of electric current. The highest discharge and charge capacities of 293 and 189 mAh g^{-1}, respectively, were obtained

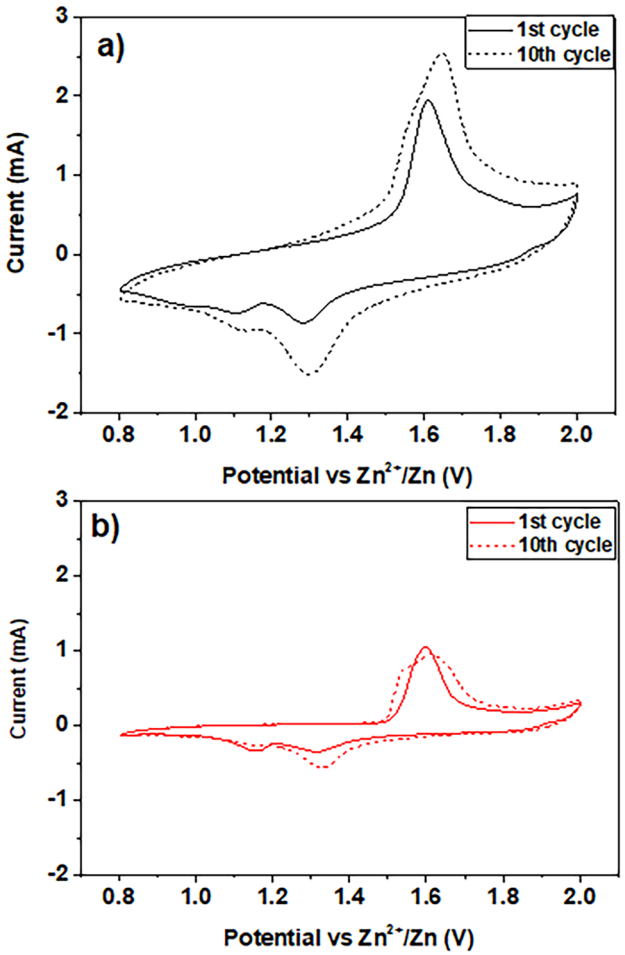

Fig. 4 Cyclic voltammetric curves of the δ-MnO_2 cathodes of ZIB using 1 M $ZnSO_4$/0.05 M $MnSO_4$ aqueous electrolyte at 0.5 mV s^{-1}. **a** δ-MnO_2_C and **b** δ-MnO_2_R

at a current density of 20 mA g^{-1}. The discharge curve reveals a change in the average sloping plateau at 1.25 V, consistent with the enhancement of the electrode/electrolyte contact area promoted by nanosized pores [17]. The electrode capacity decreases as the energy demand increases, falling to 43 and 46 mAh g^{-1} when it is charged/discharged at a high current density of 1000 mA g^{-1}. The charge profiles for all tested current densities have a similar trend, and no evident changes are observed on the slope. The rate capabilities of δ-MnO_2_C at different current densities are shown in Fig. 5b. At low current density (20 mA g^{-1}), a significant difference between the discharge/charge capacities is observed, which is associated with the material property of accepting or releasing zinc ions in deeper sites of their structure. This difference decreases as the current density increases and can

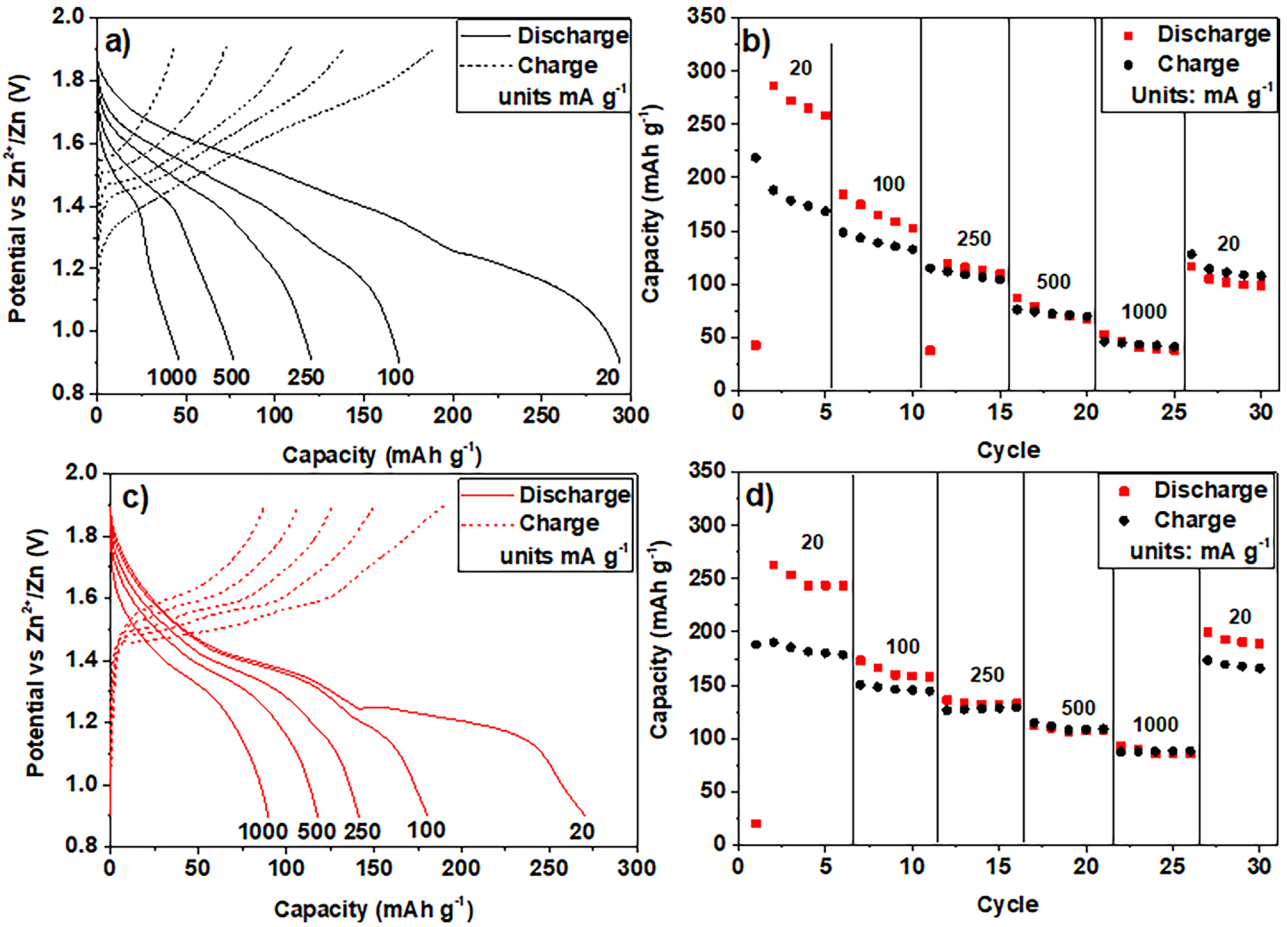

Fig. 5 Galvanostatic discharge–charge curves of the Zn/δ-MnO_2 Swagelok cell at different current densities. **a** δ-MnO_2_C and **c** δ-MnO_2_R. Rate capabilities of ZIB with δ-MnO_2 cathodes in 1 M $ZnSO_4$/0.05 M $MnSO_4$ aqueous electrolyte. **b** δ-MnO_2_C and **d** δ-MnO_2_R

be attributed to zinc ions located on more external and accessible sites on δ-MnO_2 can diffuse into the electrolyte at high energy demands. After cycling high current densities, the electrode loses approximately 60% of its initial capacity. Applying a load of 20 mA g^{-1} once more, it is observed that the charge capacity is slightly higher than the discharge capacity; this is due to the zinc ions located deeper in δ-MnO_2 pores being able to migrate and participate in the diffusion towards the anode in the charging process. The δ-MnO_2_R cathode registered discharge/charge capacities of 270 and 190 mAh g^{-1}, respectively. The discharge curve (Fig. 5c) shows two sloping plateaus at 1.4 and 1.23 V, suggesting the enhancement of the electrode/electrolyte contact area, promoted by nanosized pores, and the stable ion insertion properties of the δ-MnO_2 cathode [34]. The electrode capacity falls to 87 and 89 mAh g^{-1} when charged/discharged at 1000 mA g^{-1}. The charge profiles for all tested current densities have a similar trend, and a change in the sloping plateau at 1.6 V is observed on the slope, which confirms the stability of the extraction process of Zn ions from δ-MnO_2. The rate capabilities of the δ-MnO_2_R cathode measured at different current densities show the same trend as the previous electrode. However, the loss of capacity after being cycled at high current densities is only 26%. The discharge/charge capabilities continue with the initial trend where discharge is larger than charge capacity (Fig. 5d).

Electrochemical impedance spectroscopy was used to obtain insights into the charge transfer processes and their changes after the galvanostatic cycling processes. Electrochemical reactions such as double-layer formation and adsorption to the surface all contribute to the

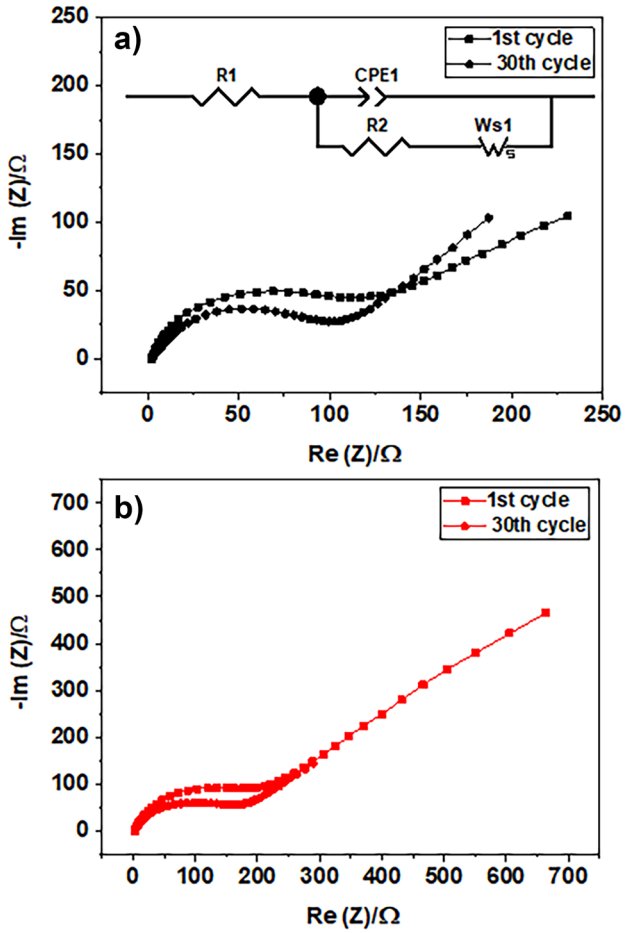

Fig. 6 Electrochemical impedance spectra of fresh and cycled cathodes of ZIB. **a** δ-MnO_2_C and **b** δ-MnO_2_R; equivalent circuit (inset)

surface cathode impedance. The Nyquist plots for analyzed electrodes are presented in Fig. 6. In both spectra, two distinct regions are observed. First, a depressed semi-circle in the high and medium frequencies related to the charge transfer on the active material surface, and second, a sloping line (~ 45°) associated with mass transport by the diffusion processes of Zn^{2+} ions inside the host material. For the δ-MnO_2_C cathode (Fig. 6a), impedance spectra before cycling show a higher charge transfer resistance ($R_2 = R_{CT}$) than those measured after the cycling process (113.2 and 99.51 Ω, respectively). The gradual activation process improves charge transfer and is also reflected in the low-frequency region with the change in the slope and decrease of Warburg diffusion impedance Z_W from 89.13 to 75.05 Ω, respectively. Since electron transfer reaction only occurs on the particle surface, the process of ion movement inside the crystals is controlled by solid-state diffusion. Figure 6b shows δ-MnO_2_R cathode impedance spectra, where it is observed that after 30 charge/discharge cycles at different loads, R_{CT} slightly decreases compared to the previously analyzed electrode 174.5 and 165 Ω before and after, respectively. There is no perceptible change in the cathode behavior, and the slope of Z_W checks it, which is the same for the measurements before and after being cycled. The highest values for R_{CT} and Z_W obtained for this cathode suggest a slower charge transfer and mass transport of Zn^{2+} ions inside the MnO_2 tunnels. However, the process proves to be more stable for charge/discharge cycling at different loads, which is reflected in a lower loss of capacity. The electrical parameters calculated for equivalent circuit fitting are summarized in Table 5.

Table 5 Equivalent circuit data from fitted impedance spectra of δ-MnO_2 cathodes before and after galvanostatic charge/discharge cycling

Sample		R_s (Ω)	R_{CT} (Ω)	$CPE_{CT} \times 10^4$ (F)	Z_W (Ω)
δ-MnO_2_C	Before	2.33	113.2	1.651	89.13
	After	2.4	99.51	1.233	75.05
δ-MnO_2_R	Before	1.98	174.5	0.296	376.1
	After	2.33	165	2.01	109

The stability tests of secondary Zn/MnO_2 assembled batteries were performed by 1000 charge/discharge cycles at 1000 mA g^{-1}. The charge/discharge cycles were not done in a row. In our case, to ensure the cathode stability, after fully charging the battery, it remained at rest for 5 min before starting the discharge cycle. Once the battery was completely discharged, it again remained at rest (5 min) before starting the charging cycle, and so on. Figure 7 shows the plots for the long-stability test and coulombic efficiency. The battery assembled with the δ-MnO_2_C cathode initially showed discharge/charge capacities of 52.9 and 46.1 mAh g^{-1}, respectively. After 1000 discharge/charge cycles, the capacities dropped to 39.17 and 35 mAh g^{-1}, respectively, with an approximate capacity loss of 2.04 µAh per cycle and a coulombic efficiency of 89.43%. In the case of the δ-MnO_2_R cathode has the same initial capacities for discharge and charge (93 mAh g^{-1}), but after 1000 discharge/charge cycles, the capacities drop to 84.39 and 81.4 mAh g^{-1}, respectively, with an approximate capacity loss of 3.4 µAh per cycle and a coulombic efficiency of 96.45%. Then the pauses between discharge/charge processes are essential to maintain the cathode stability.

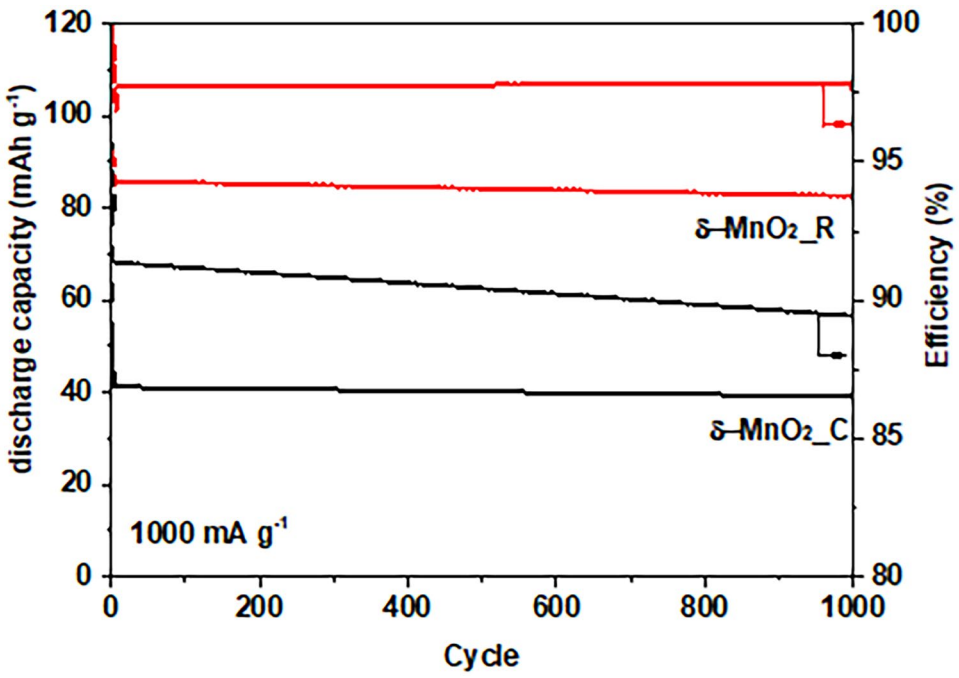

Fig. 7 Long-term cycling performance and coulombic efficiency of Zn/δ-MnO_2 secondary batteries at 1000 mA g^{-1}

Conclusions

Nanostructured δ-MnO_2 was prepared by a low-temperature interfacial synthesis using crystallized potassium permanganate obtained from recycling cathodic paste of exhausted Zn/C primary cells. The effect of the presence of sodium during the synthesis drives a change in morphology compared with the material synthesized using a permanganate reagent. This change is also reflected in a surface area and pore size decrease, maintaining the crystal structure of δ-MnO_2. Both materials were tested as cathodes Zn^{2+} ion batteries. Galvanostatic cycling showed initial high discharge/charge capacities of 289 and 189 mAh g^{-1}, respectively, for δ-MnO_2 synthesized from crystallized $KMnO_4$, slightly higher than those prepared from reagent permanganate (270 and 190 mAh g^{-1}, respectively). After the galvanostatic discharge/charge cycling, the δ-MnO_2 synthesized from crystallized permanganate lost 60% of its initial capacity after cycling at different charges. Compared to 26% of δ-MnO_2 synthesized from reagent permanganate, the long-term stability test shows that both batteries can retain between 85 and 96% of their capacity after 1000 discharge/charge cycles at a high load such as 1000 mA g^{-1}, where pauses between discharge/charge processes are essential to maintain the cathode stability. Our results indicate that it is possible to obtain active materials with high storage capacities from recycling activities and that interfacial synthesis, being a low-energy process, is attractive to produce these materials. These achievements support the sustainability of using a primary cell residue to get an electric energy storage device again.

Acknowledgements The authors thank Ignacio A. Rivero, E. A. Reynoso-Soto, S. Perez-Sicairos, and M. Eloisa Aparicio Ceja for the technical assistance.

Declarations

Conflict of interest The authors declare no competing interests.

References

1. Winter M, Brood RJ (2004) What are batteries, fuel cells, and supercapacitors. Chem Rev. https://doi.org/10.1021/cr020730k
2. Manthiram A (2017) An outlook on lithium ion battery technology. ACS Cent Sci. https://doi.org/10.1021/acscentsci.7b00288
3. Liang Y, Zhao C-Z, Yuan H, Chen Y, Zhang W, Huang J-Q, Yu D, Liu Y, Titrici M-M, Chueh Y-L, Yu H, Zhang Q (2019) A review of rechargeable batteries for portable electronic devices. InfoMat. https://doi.org/10.1002/inf2.12000
4. Wang Y, Song Y, Xia Y (2016) Electrochemical capacitors: mechanism, materials, systems, characterization, and applications. Chem Soc Rev. https://doi.org/10.1039/C5CS00580A
5. Prasad GG, Shetty N, Thakur S, Bommegowda R, Bommegowda KB (2019) Supercapacitor technology and its applications: a review. IOP Conf Ser: Mater Sci. https://doi.org/10.1088/1757-899X/561/1/012105
6. Soloveichik GL (2015) Flow batteries: current status and trends. Chem Rev. https://doi.org/10.1021/cr500720t
7. Ye R, Henkensmeier D, Yoon SJ, Huang Z, Kim DK, Chang Z, Kim S, Chen R (2018) Redox flow batteries for energy storage: a technology review. J Electrochem En Conv Stor doi 10(1115/1):4037248

8. Ding Y, Guo X, Yu G (2020) Next-generation liquid metal batteries based on the chemistry of fusible alloys. ACS Cent Sci. https://doi.org/10.1021/acscentsci.0c00749
9. Hwang J-Y, Myung S-T, Sun YK (2017) Sodium-ion batteries: present and future. Chem Soc Rev. https://doi.org/10.1039/C6CS00776G
10. Perveen T, Siddiq M, Shahzad N, Ihsan R, Ahmad A, Shahzad MI (2020) Prospects in anode materials for sodium ion batteries — a review. Renew Sust Energy Rev. https://doi.org/10.1016/j.rser.2019.109549
11. Hosaka T, Kubota K, Hameed AS, Komaba S (2020) Research development on K-ion batteries. Chem Rev. https://doi.org/10.1021/acs.chemrev.9b00463
12. Rajagopalan R, Tang Y, Ji X, Jia CH, Wang H (2020) Advancements and challenges in potassium ion batteries: a comprehensive review. Adv Func Mater. https://doi.org/10.1002/adfm.201909486
13. Sun X, Duffort V, Mehdi BL, Browning ND, Nazar LF (2016) Investigation of the mechanism of Mg insertion in birnessite in nonaqueous and aqueous rechargeable Mg-ion batteries. Chem Mater. https://doi.org/10.1021/acs.chemmater.5b03983
14. Wang F, Fan X, Gao T, Sun W, Ma Z, Yang CH, Han F, Xu K, Wang Ch (2017) High voltage aqueous magnesium ion batteries. ACS Cent Sci. https://doi.org/10.1021/acscentsci.7b00361
15. Xu Ch, Li B, Du H, Kang F (2012) Energetic zinc ion chemistry: the rechargeable zinc ion battery. Angew Chem Int Ed. https://doi.org/10.1002/anie.201106307
16. Zhang L, Chen L, Zhou X, Liu X (2014) Towards high-voltage aqueous metal-ion batteries beyond 1.5 V: the zinc/zinc hexacyanoferrate system. Adv Energy Mater. https://doi.org/10.1002/aenm.201400930
17. Alfaruqi MH, Mathew V, Gim J, Kim S, Song J, Baboo JP, Choi SH, Kim J (2015) Electrochemically induced structural transformation in a γ-MnO_2 cathode of high-capacity zinc-ion battery system. Chem Mater. https://doi.org/10.1021/cm504717p
18. He P, Quan Y, Xu X, Yan M, Yang W, An Q, He L, Mai L (2017) High-performance aqueous zinc-ion battery based on layered $H_2V_3O_8$ nanowire cathode. Small. https://doi.org/10.1002/smll.201702551
19. Corpuz RD, De Juan LMZ, Praserthdam S, Pornprasertsuk R, Yonezawa T, Nguyen MY, Khaewhom S (2019) Annealing induced a well-ordered single crystal δ-MnO_2 and its electrochemical performance in zinc-ion battery. Sci Rep. https://doi.org/10.1038/s41598-019-51692-x
20. Wang D, Wang L, Liang G, Li H, Liu Z, Tang Z, Liang J, Zhi Ch (2019) A superior δ-MnO_2 cathode and a self-healing Zn-δ-MnO_2 battery. ACS Nano. https://doi.org/10.1021/acsnano.9b04916
21. Yadav GG, Turney D, Huang J, Wei X, Banerjee S (2019) Breaking the 2 V barrier in aqueous zinc chemistry: creating 2.45 and 2.8 V MnO_2-Zn aqueous batteries. ACS Energy Lett. https://doi.org/10.1021/acsenergylett.9b01643
22. Zhang N, Cheng F, Liu J, Wang L, Long X, Liu X, Li F, Chen J (2017) Rechargeable aqueous zinc-manganese dioxide batteries with high energy and power densities. Nature Comm. https://doi.org/10.1038/s41467-017-00467-x
23. Wang X, Wang F, Wang L, Li M, Wang Y, Chen B, Zhu Y, Fu L, Zha L, Zhang L, Wu Y, Huang Y (2016) An aqueous rechargeable Zn//Co_3O_4 battery with high energy density and good cycling behavior. Adv Mater. https://doi.org/10.1002/adma.201505370
24. Wu X, Xiang Y, Peng Q, Wu X, Li Y, Tang F, Song R, Liu Z, He Z, Wu X (2017) Green-low-cost rechargeable aqueous zinc-ion-batteries using hollow porous spinel $ZnMnO_4$ as cathode material. J Mater Chem A. https://doi.org/10.1039/C7TA00100B
25. Li G, Yang Z, Jiang Y, Jin Ch, Huang W, Ding X, Huang Y (2016) Towards polyvalent ion batteries: a zinc-ion battery based on NASICON structured $Na_3V_2(PO_4)_3$. Nano Energy. https://doi.org/10.1016/j.nanoen.2016.04.051
26. Jia Z, Wang B, Wang Y (2015) Copper hexacyanoferrate with well-defined open framework as a positive electrode for aqueous zinc ion batteries. Mater Chem Phys. https://doi.org/10.1016/j.matchemphys.2014.11.014
27. Hashemzadeh F, Motlagh MMK, Maghsoudipour A (2009) A comparative study of hydrothermal and sol-gel methods in the synthesis of MnO_2 nanostructures. J Sol-Gel Sci Technol. https://doi.org/10.1007/s10971-009-1978-2
28. Zhu G, Li H, Deng L, Liu Z-H (2010) Low-temperature synthesis of δ-MnO_2 with large surface area and its capacitance. Mater Lett. https://doi.org/10.1016/j.matlet.2010.05.019
29. Xie Y, Yu Y, Gong X, Guo Y, Guo Y, Wang Y, Lu G (2015) Effect of the crystal plane figure on the catalytic performance of MnO_2 for the total oxidation of propane. CrystEngComm. https://doi.org/10.1039/C5CE00058K
30. McLarnon FR, Cairns EJ (1991) The secondary alkaline zinc electrode. J Electrochem Soc. https://doi.org/10.1149/1.2085653
31. Alkaline Primary Batteries Global Market Report 2021: COVID-19 Impact and Recovery to 2030 (2021) https://www.researchandmarkets.com/reports/5323117/alkaline-primary-batteries-global-market-report
32. Jia Z, Wang J, Wang Y, Li B, Wang B, Qi T, Wang X (2016) Interfacial synthesis of δ-MnO_2 nano-sheets with a large surface area and their application in electrochemical capacitors. J Mater Sci Tech. https://doi.org/10.1016/j.jmst.2015.08.003
33. Sotomayor FJ, Cychocz KA, Thommes M (2018) Characterization of micro/mesoporous materials physisorption: concepts and case studies. Acc Mater Suf Res 3(2):34–50
34. Alfaruqi MH, Gim J, Kim S, Song J, Pham DT, Jo J, Xiu Z, Mathew V, Kim J (2015) A layered δ-MnO_2 nanoflake cathode with high zinc-storage capacities for eco-friendly battery applications. Comm Electrochem. https://doi.org/10.1016/j.elecom.2015.08.019